JACS
JOURNAL OF THE AMERICAN CHEMICAL SOCIETY

pubs.acs.org/JACS

Article

Conformational Flexibility of Hybrid [3]- and [4]-Rotaxanes

Selena J. Lockyer, Selina Nawaz, Adam Brookfield, Alistair J. Fielding, Inigo J. Vitorica-Yrezabal, Grigore A. Timco, Neil A. Burton, Alice M. Bowen, Richard E. P. Winpenny,* and Eric J. L. McInnes*

Cite This: *J. Am. Chem. Soc.* 2020, 142, 15941−15949

Read Online

ACCESS | Metrics & More | Article Recommendations | Supporting Information

ABSTRACT: The synthesis, structures, and properties of [4]- and [3]-rotaxane complexes are reported where [2]-rotaxanes, formed from heterometallic $\{Cr_7Ni\}$ rings, are bound to a fluoride-centered $\{CrNi_2\}$ triangle. The compounds have been characterized by single-crystal X-ray diffraction and have the formulas $[CrNi_2(F)(O_2C^tBu)_6]\{(\mathbf{BH})[Cr_7NiF_8(O_2C^tBu)_{16}]\}_3$ (**3**) and $[CrNi_2(F)(O_2C^tBu)_6(THF)]\{(\mathbf{BH})[Cr_7NiF_8(O_2C^tBu)_{16}]\}_2$ (**4**), where **B** = py-$CH_2CH_2NHCH_2C_6H_4SCH_3$. The [4]-rotaxane **3** is an isosceles triangle of three [2]-rotaxanes bound to the central triangle while the [3]-rotaxane **4** contains only two [2]-rotaxanes bound to the central triangle. Studies of the behavior of **3** and **4** in solution by small-angle X-ray scattering and atomistic molecular dynamic simulations show that the structure of **3** is similar to that found in the crystal but that **4** has a different conformation to the crystal. Continuous wave and pulsed electron paramagnetic resonance spectroscopy was used to study the structures present and demonstrate that in frozen solutions (at 5 K) **4** forms more extended molecules than **3** and with a wider range of conformations.

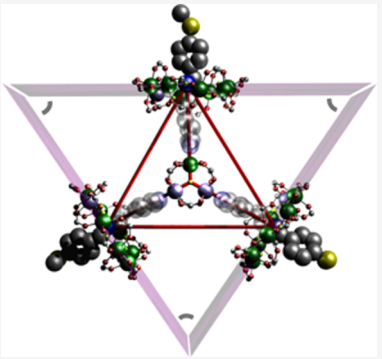

INTRODUCTION

The flexibility of supramolecular assemblies has long been of interest. For example, the rigidity of molecular capsules has been used to allow them to act as reactors to catalyze specific reactions[1] or to stabilize reactive species.[2,3] Interlocked structures such as the various knots reported[4−6] also introduce rigidity and have been proposed as means of making less flexible polymers.[7] Studying rigidity is possible using NMR spectroscopy where the species is diamagnetic; for example, the demetalated knots made by Zhang et al. show broad NMR spectra that become sharper when diamagnetic Zn^{2+} ions are added, which increases the rigidity. Studying the flexibility of interlocked structures where building blocks are paramagnetic is far harder as the NMR is paramagnetically broadened before the conformational flexibility is considered. Small-angle X-ray scattering (SAXS) has been previously used to show supramolecular assemblies are present in solution;[8,9] we have used SAXS supported by atomistic molecular dynamics simulations (AMDS) to demonstrate that a [13]-rotaxane maintained its structure in solution.[10] Here, we use SAXS on two related rotaxanes to show that the larger [4]-rotaxane has a more similar structure between solution and crystalline phases, while the [3]-rotaxane has a much more open structure in solution. The studies require the comparison of SAXS and double electron−electron resonance (DEER) spectroscopy while remembering they operate at 300 and 5 K, respectively.

We have previously reported hybrid [2]-rotaxanes where the ring is a $[Cr_7NiF_8(O_2C^tBu)_{16}]^-$ unit and the thread is a secondary ammonium with suitable sterically demanding stoppers.[11,12] If there is a pyridyl (py) head group on the thread, for example, py-$CH_2NHCH_2CH_2Ph$ (**A**), the [2]-rotaxane $(\mathbf{AH})[Cr_7NiF_8(O_2C^tBu)_{16}]$ can be used to bind to Lewis acid complexes.[13,14] Here, we extend this approach, binding [2]-rotaxanes to a fluoride-centered triangle $[CrNi_2(\mu_3\text{-}F)(O_2C^tBu)_6(HO_2C^tBu)_3]$ **1** (Figure S2, Supporting Information), which has a labile terminal ligand (HO_2C^tBu) at each vertex. By small changes in the synthesis [3]- and [4]-rotaxanes can be made and show very different solution flexibility.

Such assemblies have been proposed as routes to implement qubit gates. Both the $\{Cr_7Ni\}$ ring and the $\{CrNi_2\}$ triangle have $S = {}^1/_2$ ground states, but with very different *g*-values of ca. 1.8 and 2.5.[15] This gives supramolecular assemblies where we can potentially address different components by EPR spectroscopy. This has also been investigated.

RESULTS

Synthesis and Structural Analysis. The parent $\{CrNi_2\}$ triangle $[CrNi_2(\mu_3\text{-}F)(O_2C^tBu)_6(HO_2C^tBu)_3]$ (**1**; Figure S2) was prepared as reported previously.[15] Attempts to coordinate $(\mathbf{AH})[Cr_7NiF_8(O_2C^tBu)_{16}]$[13] to **1** were unsuccessful, probably because of the thread being too short, leading to repulsive steric interactions between the components. Hence, we made py-$CH_2CH_2NHCH_2C_6H_4SCH_3$ (**B**), which has a greater

Received: June 19, 2020
Published: August 21, 2020

https://dx.doi.org/10.1021/jacs.0c06547
J. Am. Chem. Soc. 2020, 142, 15941−15949

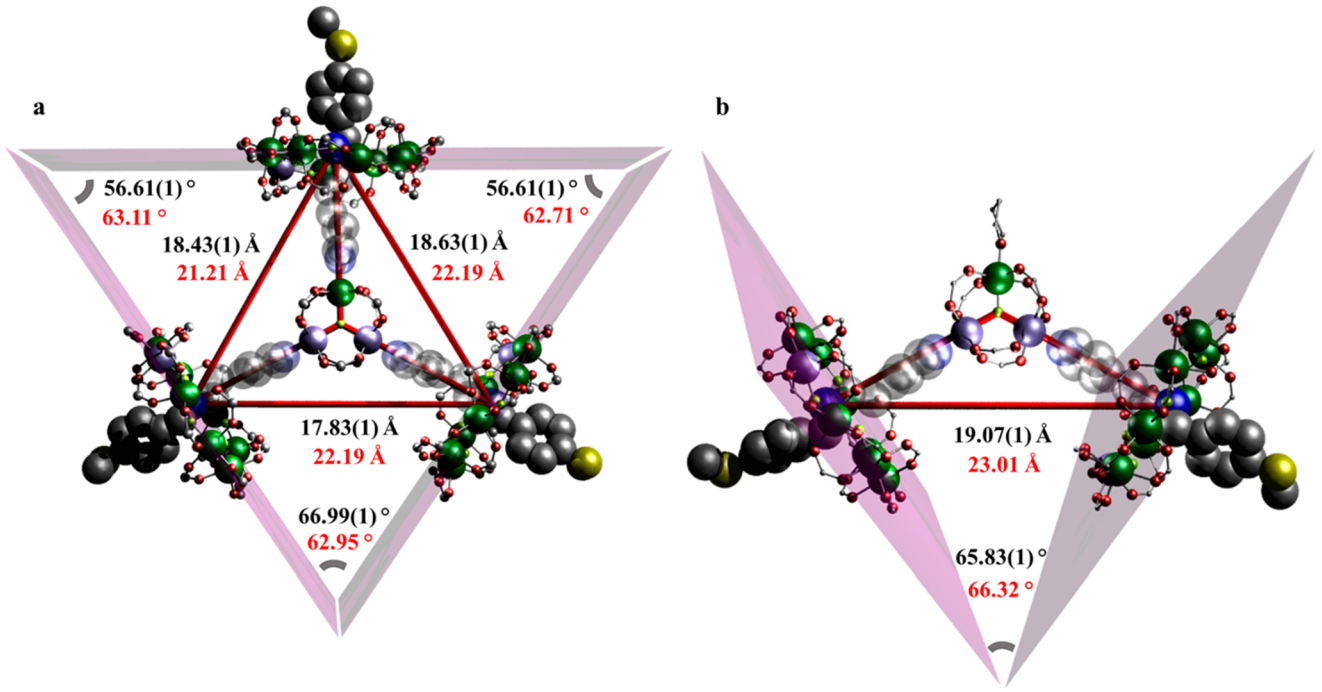

Figure 1. Structures of **3** and **4** in the crystal, with select metric parameters indicated (black, XRD; red, AMDS). (a) **3** showing angles between the mean planes of the $\{Cr_7Ni\}$ rings and the distances between N atoms of secondary ammonium groups; (b) **4** showing angles between the mean planes of the $\{Cr_7Ni\}$ rings and the distances between N atoms of secondary ammonium groups. Colors: Cr, green; Ni, purple; O, red; F, yellow; N, blue; C, silver; S, dull yellow. H atoms and methyl groups of pivalates excluded for clarity.

distance between the secondary amine site and the pyridyl head group.[16] A [2]-rotaxane can then be prepared, of formula $(\mathbf{BH})[Cr_7NiF_8(O_2C^tBu)_{16}]$ (**2**); the thread is protonated at the amine site during this reaction (Figure S3).

Reaction of 3 equiv of **2** with **1** in THF at 40 °C produces the 3:1 $\{Cr_7Ni\}/\{CrNi_2\}$ adduct $[CrNi_2(F)(O_2C^tBu)_6]\{(\mathbf{BH})[Cr_7NiF_8(O_2C^tBu)_{16}]\}_3$ **3** (Figure 1a), as shown by X-ray diffraction. The structure contains three molecules of **2** each bound to a metal site of the central triangle **1** via the py head groups of the $(\mathbf{BH})^+$ threads. Compound **3** is therefore a [4]-rotaxane. It crystallizes with a 2-fold axis of rotation passing through the molecule and therefore the asymmetric unit comprises half of the complete molecule.

In the central $\{CrNi_2\}$ triangle each metal ion is in a pseudo-octahedral geometry, with the pyridyl bound trans to the central μ_3-fluoride, which is planar (Ni−F−Cr and Ni−F−Cr angles all around 120°). In the solid state, the pyridyl groups are almost perpendicular to the $\{CrNi_2\}$ plane; angles between the py and $\{CrNi_2\}$ planes vary from 75.14(1) to 80.88(1)°. Each $\{Cr_7Ni\}$ ring sits about the secondary ammonium group (N^{am}) of $(\mathbf{BH})^+$, with hydrogen bonds to two of the bridging fluorides on the interior of the ring.

The Cr^{III} site in the triangle is disordered over the three sites. Similarly, in the $\{Cr_7Ni\}$ rings, the Ni^{II} site is disordered over all eight metal positions. Although elemental analysis gives a slight excess of Ni with a Ni/Cr ratio of 6:22 (5:22 expected for a **2**/$\{CrNi_2\}$ ratio of 3:1), EPR spectroscopy unequivocally demonstrates that there is no scrambling of the metal ions; that is, all the rings are $\{Cr_7Ni\}$ and all the triangles are $\{CrNi_2\}$ (see below).

If the reaction is carried out using 2 equiv of **2** to **1** and in THF at 20 °C, we isolate the 2:1 $\{Cr_7Ni\}/\{CrNi_2\}$ adduct where only two sites of **1** have been substituted by **2** and the third site is occupied by a THF molecule. The product is a [3]-rotaxane $[CrNi_2(F)(O_2C^tBu)_6(THF)]\{(\mathbf{BH})[Cr_7NiF_8(O_2C^tBu)_{16}]\}_2$ (**4**; Figure 1b). X-ray diffraction shows that the THF substituted metal site of the $\{CrNi_2\}$ triangle has a shorter M−F bond distance of 1.89(3) Å cf. 2.06(1) and 2.06(1) Å and hence the Cr^{III} site is localized. The μ_3-F^- of the triangle is again planar with Ni−F−Cr and Ni−F−Cr angles near 120°. The planes of the py groups are almost perpendicular to the $\{CrNi_2\}$ plane, with dihedral angles of 77.48(1) and 84.04(1)°, which are similar to those of **3**.

To define the shape of the two supramolecules, we report some simple metric parameters (Figure 1, Table 1). First, we consider the distance from the central fluoride in each case to the protonated secondary ammonium in each thread about which the $\{Cr_7Ni\}$ rings are grown: this is the N^{am}...F distance for each thread. We then consider the N^{am}...N^{am} distances; these define the edges of the triangle of $\{Cr_7Ni\}$ rings in **3**. The

Table 1. Metric Parameters Defining the Shape of the [*n*]-Rotaxanes

	3		4	
	X-ray	AMDS	X-ray	AMDS
N^{am}..F distance/Å	10.56(1) 10.57(1) 10.57(1)	10.31(1) 10.31(1) 10.31(1)	10.82(1) 10.84(1)	10.31(1) 10.31(1)
N^{am}..N^{am} distance/Å	17.83(1) 18.43(1) 18.83(1)	21.21(1) 21.21(1) 22.19(1)	19.07(1)	23.01(1)
Ring..ring angle/°	56.61(1) 56.61(1) 66.99(1)	62.71(1) 62.95(1) 63.11(1)	65.83(1)	66.32(1)

https://dx.doi.org/10.1021/jacs.0c06547
J. Am. Chem. Soc. 2020, 142, 15941−15949

angles between the mean planes of the {Cr_7Ni} rings on each [2]-rotaxane are given as the ring···ring angles. In each case the mean plane of the ring is essentially perpendicular to the thread passing through it.

The X-ray diffraction results show that **3** contains an approximately isosceles triangle of {Cr_7Ni} rings, with one ring···ring angle noticeably more obtuse than the other two. The N^{am}...F distances are constant. For **4** the angle between the two rings is similar to the most obtuse angle for **3** and the N^{am}...N^{am} and N^{am}...F distances are both longer than those in **3**.

Atomistic Molecular Dynamic Simulations (AMDS) and Small- Angle X-ray Scattering (SAXS). To study the stability and structures of **3** and **4** in solution, we performed atomistic molecular dynamic simulations (AMDS) with an all-atom simulation of the two crystal structures (in a concentrated THF solution) using GROMACS 5.1.4 molecular dynamics package.[17,18] The crystal structures of **3** and **4** were parametrized using the AMBER95 force field, augmented by parameters consistent with the General Amber force field.[19] Eight nanometer cubic simulation boxes were set up containing a single molecule of **3** or **4** in a solution of 2774 THF molecules and run in an NPT ensemble for the solvent density to reach ~890 kg m^{-3}.

The calculated AMDS structures were then compared with experimental solution structure information from SAXS data. SAXS profiles calculated from the AMDS structures used Hartree−Fock scattering factors, with 100 nm boxes and X-ray wavelength of 0.154209 nm. Experimental and AMDS-model calculated SAXS intensity profiles (plotted as $\ln[I(q)]$ (a.u.), where q (Å) is the scattering vector) are in Table S2 and Figure S12. The corresponding pair distribution functions $P(r)$ for **3** and **4** are in Figure 2.

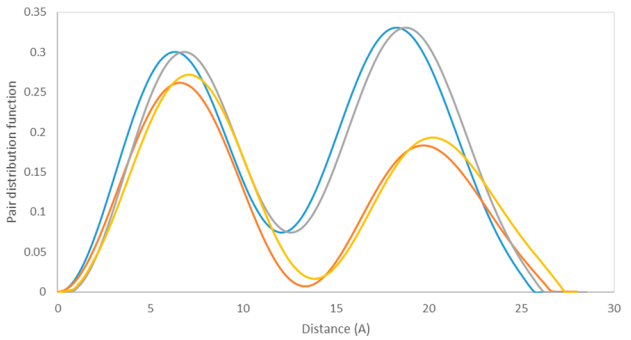

Figure 2. Observed and calculated SAXS data for **3** and **4**, in THF solution at 20 °C. The experimental data are shown in blue and red, respectively, for **3** and **4**. The calculated traces are shown in gray and yellow, respectively, for **3** and **4**.

There is remarkable agreement between AMDS and SAXS for both **3** and **4**, demonstrating that both structures are stable in THF solution (Figure 2). The very slight discrepancies between the experimental SAXS and corresponding pair distribution function is less than 1 Å, for both **3** and **4**, which can be accountable by force field errors. This discrepancy is also seen in the radius of gyration (R_g) values shown in Table S2. The radius of gyration for the simulated structures of both **3** and **4** are slightly higher, indicating the calculated structures are more extended in comparison to the experimental data.

The $P(r)$ distributions are dominated by a short distance (ca. 6 Å) and a longer distance at ca. 18 and 20 Å for **3** and **4**, respectively. The longer distance can be attributed to the distances between {Cr_7Ni} rings. Note that this inter-ring distribution has greater amplitude for **3** than for **4**, consistent with the 3:1 vs 2:1 {Cr_7Ni}/{$CrNi_2$} stoichiometries. The shorter distances within the peak centered at ca. 7 Å are due to distances within individual {Cr_7Ni} rings, agreeing with the crystallographic values that range from 3.3(1) Å (neighboring sites) to 8.7(1) Å (antipodal sites). The combination of AMDS/SAXS confirm that **3** and **4** are distinct compounds in solution and, for example, **3** does not exist in equilibrium with **4** and a dissociated [2]-rotaxane **2**.

The AMDS structures calculated by molecular dynamics are also in good agreement with the single-crystal structures (see Table 1 for selected metric parameters) but with some subtle and intriguing variations. Compound **3** is noticeably more equilateral in solution, with the ring···ring angles all very similar. While the three angles in the crystal structure sum to close to 180°, in the AMDS structure they sum to an average of 189° over the last 5 ns of the simulations, which corresponds to the rings tilting away from the normal to the {$CrNi_2$} plane in solution. The N^{am}...F distances are shorter but N^{am}...N^{am} distances are 17% longer. These observations indicate that the rings are packed together more closely than they would like in the crystal and the structure relaxes in solution. Compound **4** has a very similar ring···ring angle in solution and crystal structure (Table 1), but the N^{am}...N^{am} distance is 20% longer in solution than in the crystal. This again suggests that the structure in the solution has relaxed compared with the crystal structure.

Electron Paramagnetic Resonance Spectroscopy. Continuous wave (c.w.) Q-band (ca. 34 GHz) EPR spectroscopy measurements were performed on **3** and **4** at 5 K for powder samples and for frozen 3 mM toluene solutions. The spectra are dominated by the $S = {}^1/_2$ ground states of the {Cr_7Ni} and {$CrNi_2$} components that arise from internal antiferromagnetic coupling.

The powder spectra for **3** and **4** (Figure S4; left and right, respectively) both contain two slightly asymmetric features, centered on 995 and 1382 mT. The frozen solution spectra (Figure 3) have narrower line widths, which for both **3** and **4**

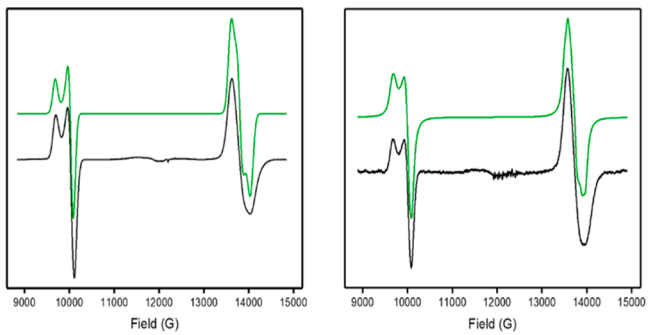

Figure 3. c.w. Q-band EPR (ca. 34 GHz) spectra for a 3 mM solution sample in dry toluene for **3** (left) and **4** (right) at 5 K. Black, experimental; green, simulation.

reveal approximately axial splitting of the lower field feature, while the higher field feature remains largely unchanged. The spectra were simulated[20] using a spin-Hamiltonian incorporating only the individual **g** matrices for the $S = {}^1/_2$ {$CrNi_2$} and {Cr_7Ni} components and an isotropic exchange interaction:

https://dx.doi.org/10.1021/jacs.0c06547
J. Am. Chem. Soc. 2020, 142, 15941−15949

$$\hat{H} = \mu_B \hat{S}^{CrNi2} \cdot \mathbf{g}^{CrNi2} \cdot \mathbf{B} + \sum \mu_B \hat{S}^{Cr7Ni} \cdot \mathbf{g}^{Cr7Ni} \cdot \mathbf{B} - 2J \sum \hat{S}^{CrNi2} \cdot \hat{S}^{Cr7Ni}$$

where the summation is over three (compound **3**) or two (compound **4**) $\{Cr_7Ni\}$ centers.

For the frozen solutions, the lower field feature due to $\{CrNi_2\}$ can be fitted with for **3**, $g_{x,y,z}$ = 2.425, 2.425, 2.520; for **4**, $g_{x,y,z}$ = 2.420, 2.425, 2.515. These agree well with the spectra found for **1**.[15] The high field feature due to $\{Cr_7Ni\}$ can be fitted with **3**, $g_{x,y,z}$ = 1.785, 1.778, 1.730 ; and **4**, $g_{x,y,z}$ = 1.782, 1.782, 1.740. These agree with the spectra of $\{Cr_7Ni\}$ rings.[21] Reasonable fits can be achieved with these g values for J = 0.

A slight improvement in the agreement between the simulated and observed spectra is found with the inclusion of a small exchange interaction of $|J|$ = 0.003 cm^{-1}. However, this only serves to broaden the transitions. This broadening can also be achieved by inclusion of a small (1%) g strain for each $\{Cr_7Ni\}$ component. Frozen solution spectra of **3** at lower frequencies (X- and S-band) fit better with the g-strain model than with the small, but unresolved J model (Figure S5). We conclude that there are no measurable features due to exchange coupling in the c.w. EPR spectra.

Pulsed EPR spectroscopy (Q-band, 3 K) was used to measure the phase memory times (T_m) for **3** and **4** using standard Hahn echo decay measurements: [$^{\pi}/_2$−τ−π−τ−echo]. Spin−lattice relaxation (T_1) measurements were carried out by inversion recovery [π−T−$^{\pi}/_2$−τ−π−τ−echo]. We have also done comparable measurements on the isolated triangle $[CrNi_2(F)(O_2C^tBu)_6(py)_3]$ **5**.[15] Measurements were made at magnetic fields (B_0) corresponding to resonances of the $\{Cr_7Ni\}$ ring and the g_{xy} and g_z features for the $\{CrNi_2\}$ triangle (Table 2 and Figure S6). The phase memory (T_m) times are similar for all components in both structures at around 700 ns, with the exception of the g_z values for the $\{CrNi_2\}$ fragment in **3** and **4**, which is shorter (ca. 570 ns), and shorter than that in the isolated $\{CrNi_2\}$ triangle **5**. The T_1 times vary more and the times for the isolated triangle are significantly longer than those for the $\{CrNi_2\}$ g values in **3** and **4** (Table 2 and Figures S7 and S9).

Table 2. Q-Band Relaxation Times for 3, 4, and 5 Measured at 3 K in 0.2 mM Solution in Toluene

compound	g value	assignment	T_m (ns)	T_1 (μs)
3	2.41	g_{xy} $\{CrNi_2\}$	713 (0.42)	172 (0.38)
3	2.47	g_z $\{CrNi_2\}$	562 (2.96)	108 (1.78)
4	2.41	g_{xy} $\{CrNi_2\}$	689 (2.46)	258 (3.34)
4	2.47	g_z $\{CrNi_2\}$	578 (3.61)	165 (1.43)
5	2.41	g_{xy} $\{CrNi_2\}$	863 (0.4)	840 (17)
5	2.47	g_z $\{CrNi_2\}$	848 (0.5)	813 (24)
3	1.78	$\{Cr_7Ni\}$	713 (0.42)	62 (0.38)
4	1.78	$\{Cr_7Ni\}$	826 (0.56)	108 (0.75)

ESEEM modulations are observed in the Hahn echo decay measurements at B_0 values corresponding to the $\{CrNi_2\}$ but not for the $\{Cr_7Ni\}$ components. Fourier transforms of the time-domain data for the $\{CrNi_2\}$ measurements are similar for **3** and **4**, with a series of low-frequency (<10 MHz) peaks (Figure S8).

Double Electron−Electron Resonance Spectroscopy (DEER). DEER is an established method for measuring interspin distances in biological systems.[22−24] Previously, we have reported DEER measured on supramolecular compounds containing two $\{Cr_7Ni\}$ rings and demonstrated that we could measure the weak $\{Cr_7Ni\}\cdots\{Cr_7Ni\}$ interactions.[25] In those studies the two rings were coplanar, linked along the normal to the planes of the rings, either by forming a [3]-rotaxane, or linked covalently via a diamagnetic bridge. In **3** and **4** the planes of the rings make angles of ∼60° to one another (see Table 1), which introduces further structural complexity to interpreting the results.

Four-pulse DEER experiments were performed on solutions of **3** and **4** to probe the $\{Cr_7Ni\}\cdots\{Cr_7Ni\}$interactions. The pump pulse was set on the $\{Cr_7Ni\}$ maximum (B_0 = 1373 mT) with the observer pulse set 100 MHz higher in frequency than the pump pulse. For both compounds, we observe oscillations in the DEER traces (Figures 4 and 5). For **3**, Fourier transformation of the background-corrected data gives a frequency domain spectrum with peaks at ±5 MHz, with a slight shoulder at ±3 MHz, and broad wings between ±10−30 MHz. For **4**, we obtain similar oscillations but with weaker modulation depth, giving a frequency domain spectrum with two distinct peaks at ±2.5 and ±5 MHz. There appears to be less intensity in the wings.

Two analysis methods were used to extract interspin distance distribution from the time traces. First, a Tikhonov regularization[26] using the orientation-independent kernel in DeerAnalysis,[27] with a correction for the g values corresponding to the pump and detection frequencies, yields three main components for **3** (Figure 4c) and gives four clear groups of distances for **4** (Figure 5c).

Second, a simulation library approach was used (see Supporting Information). A series of geometric models were developed based on the crystal structures of **3** and **4**. For each model the expected orientation-dependent DEER trace for pairwise ring−ring dipolar interactions was calculated using an algorithm described elsewhere.[28] The unpaired spin density in each $\{Cr_7Ni\}$ was equally distributed on each metal ion, reflecting the fact that the Ni position in the ring is not localized. The calculations used the anisotropic g values from c.w. spectra, and the mw pulse and magnetic field parameters used in the experimental acquisition. This library of simulated DEER traces was fitted to the experimental data traces using an iterative procedure over 50 iterations, similar to that described elsewhere.[29] The time and frequency domain fits and the corresponding distance distributions, presented as both the inter-ring M···M distances and ring centroid-to-centroid distances, are presented in Figures 4 and 5.

Power scaling of the DEER data for **3** was used to test for the presence of significant multispin effects and ghost peaks in the extracted distance distribution.[30] The contribution of the multispin effects to the data set is vanishingly small (see Supporting Information): this is because the inversion efficiency of the DEER experiment is very low (λ = 0.0135). This validates the application of the pairwise analysis approaches described above for **3**. The greater modulation depth for **3** than for **4** is consistent with the presence of three $\{Cr_7Ni\}$ rings in the former and two in the latter.[31]

It is not possible to probe the $\{Cr_7Ni\}\cdots\{CrNi_2\}$ interactions by DEER due to the very different g values leading to spectra that do not overlap and the limited bandwidth of the resonator used (ca. 200 MHz when overcoupled).

https://dx.doi.org/10.1021/jacs.0c06547
J. Am. Chem. Soc. 2020, 142, 15941−15949

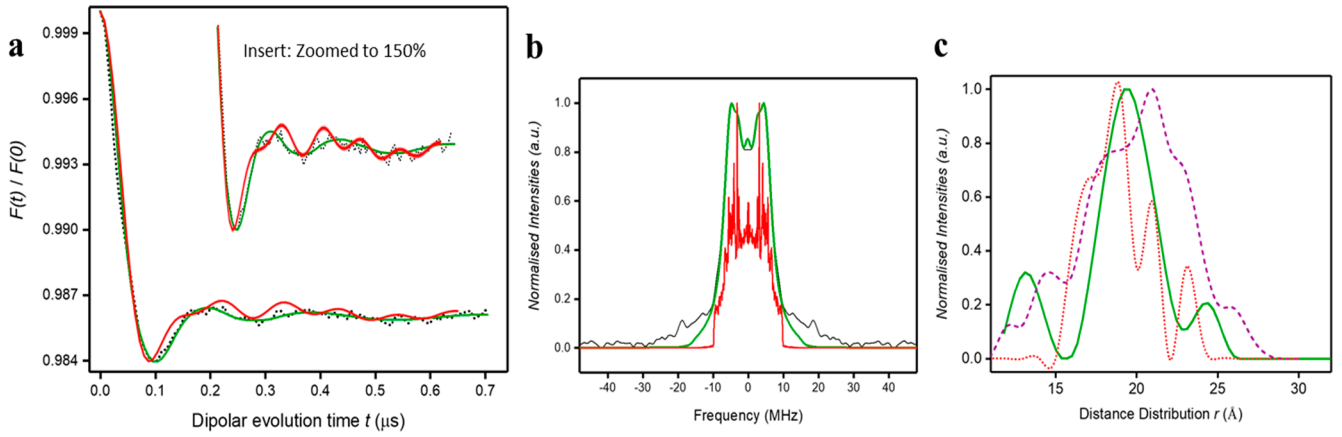

Figure 4. (a) Q-Band experimental DEER trace of **3**, after background subtraction (black crosses, 0.2 mM solution in dry and degassed toluene at 3 K) and fitted data; using DeerAnalysis (solid green line) and using an iterative orientation procedure (solid red line), with vertical enlargement (insert). A four-pulse DEER sequence was used, with the ELDOR pulse at the $\{Cr_7Ni\}$ maximum (B_0 = 1373 mT) and observation pulse positioned at +100 MHz. Pulse lengths were 20 and 40 ns for $^{\pi}/_2$ and π, respectively, with τ_1 = 200 ns and τ_2 = 1000 ns. (b) Pake pattern from Fourier transformation of dipolar evolution (solid black line); fitted data using DeerAnalysis (solid green line) and the iterative orientation procedure (solid red line). (c) Distance distribution using Tikhonov regularizations in DeerAnalysis and corrected g values (solid green line), and from the model from the iterative orientation procedure showing inter-ring metal−metal distances (dashed purple line) and ring centroid−centroid distances (dotted red line).

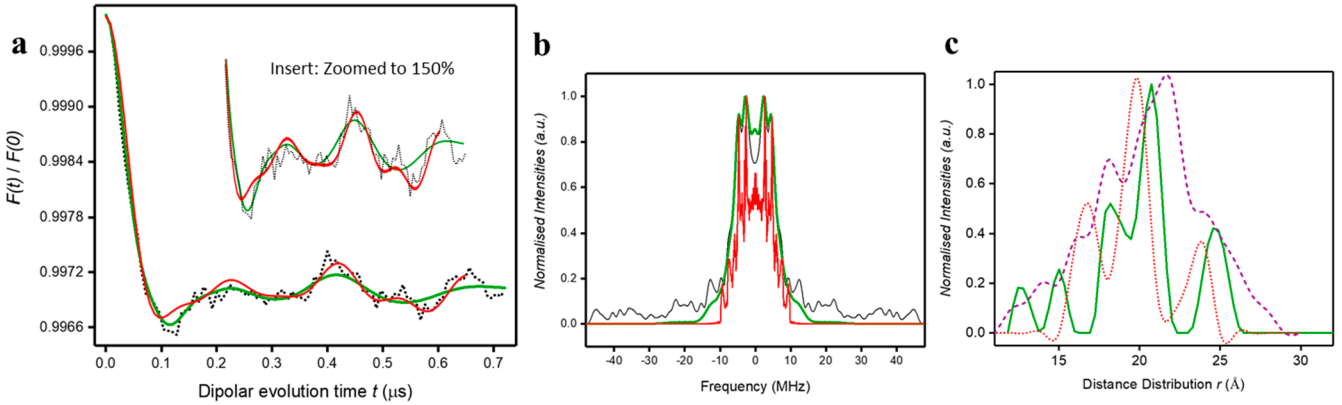

Figure 5. (a) Q-band experimental DEER trace of **4**, after background subtraction (black crosses, 0.2 mM solution in dry and degassed toluene at 3 K) and fitted data; using DeerAnalysis (solid green line) and using an iterative orientation procedure (solid red line), with vertical enlargement (insert). A four-pulse DEER sequence was used, with the ELDOR pulse at the $\{Cr_7Ni\}$ maximum (B_0 = 1373 mT) and observation pulse positioned at +100 MHz. Pulse lengths were 20 and 40 ns for $^{\pi}/_2$ and π, respectively, with τ_1 = 200 ns and τ_2 = 1000 ns. (b) Pake pattern from Fourier transformation of dipolar evolution (solid black line); fitted data using DeerAnalysis (solid green line) and the iterative orientation procedure (solid red line). (c) Distance distribution using Tikhonov regularizations in DeerAnalysis and corrected g values (solid green line), and from the model from the iterative orientation procedure showing inter-ring metal−metal distances (dashed purple line) and ring centroid−centroid distances (dotted red line).

DISCUSSION

The c.w. EPR spectra prove unambiguously that there is no scrambling of metal ions in either the $\{Cr_7Ni\}$ or $\{CrNi_2\}$ components in **3** or **4**. We observe only the $S = {}^1/_2$ ground states of either component, which arises from internal antiferromagnetic coupling. Any scrambling of the metal ions would lead to the observation of other spin states. There is no evidence of spin···spin interaction between the $\{Cr_7Ni\}$ and $\{CrNi_2\}$ components in the c.w. EPR data; hence, any interaction must be very weak with respect to the intrinsic line widths. The c.w. EPR spectra of **3** and **4** are very similar in powder and frozen solution. However, given the lack of resolution of any interaction, this does not prove that the structure is stable in solution (only that the separate components are stable). This evidence comes from the SAXS and AMDS data, and also from DEER measurements that reveal $\{Cr_7Ni\}\cdots\{Cr_7Ni\}$ interactions.

The weak coupling regime between $\{Cr_7Ni\}$ or $\{CrNi_2\}$ is further proven from electron spin relaxation measurements on the separate components.

Electron Spin Relaxation. The T_1 and T_m values for the $\{Cr_7Ni\}$ components of **3** and **4** (ca. 60−100 and 700−800 ns, respectively, at 3 K) are in the range observed for the free ring and in other supramolecular assemblies containing this fragment (Table 2; some caution needs to be taken when comparing data measured at the Q- and X-band).[14] Hence, there seems to be relatively little variation in the $\{Cr_7Ni\}$ relaxation regardless of the complexity of the supramolecular structure (we have measured similar T_m in a complex bearing 12 $\{Cr_7Ni\}$ rings).[10]

https://dx.doi.org/10.1021/jacs.0c06547
J. Am. Chem. Soc. 2020, 142, 15941−15949

The T_1 and T_m values for the $\{CrNi_2\}$ components of **3** and **4** are ca. 110−260 and 600−700 ns, respectively. Measurements on the isolated $\{CrNi_2\}$ complex $[CrNi_2F(O_2C^tBu)_6(py)_3]$ (**5**) under the same conditions give $T_1 \sim 800$ μs and $T_m \sim 800$ ns; we have chosen this complex to give a direct comparison with the pyridyl-terminated $\{CrNi_2\}$ units in **3** and **4**. Hence, in contrast to $\{Cr_7Ni\}$, incorporating $\{CrNi_2\}$ into the supramolecular structures **3** and **4** results in a significant decrease in T_1.

In the free complexes, T_1 for $\{Cr_7Ni\}$ (ca. 100 μs) is significantly shorter than that of $\{CrNi_2\}$ (ca. 800 μs). Both compounds are antiferromagnetically coupled Cr^{III}...Ni^{II} clusters that give rise to $S = {}^1/_2$ ground states. $\{Cr_7Ni\}$ is a much bigger spin system and hence has a higher density of spin states, while the exchange coupling within $\{CrNi_2\}$ is weaker,[15] leading to lower lying excited states. It would appear that the former is the dominant effect in determining the relative magnitude of T_1 in these two species. The difference between the T_1 times of the two components is much reduced in **3** and **4**. The effect of a fast relaxing spin on a slower relaxing spin depends on the relative magnitude of the coupling and the difference in resonance frequency.[32] Even where the coupling is weak, it can enhance the $1/T_1$ relaxation rate of the slow spin. This appears to be the case in **3** and **4**, where T_1 of the $\{CrNi_2\}$ components (110−260 μs) is still longer than that of the $\{Cr_7Ni\}$ rings (60−100 μs), but reduced from the free $\{CrNi_2\}$. This is also the reason for the stability of the $\{Cr_7Ni\}$ T_1 values across a wide range of supramolecular assemblies: in all these systems the rings are the fastest relaxing components.

The T_m values for the slower relaxing $\{CrNi_2\}$ components in both **3** and **4** (600−700 ns) are similar to that of isolated $\{CrNi_2\}$ (800 ns). This implies that the $1/T_1$ relaxation rate of the faster relaxing $\{Cr_7Ni\}$ spin (of the order 10^{-1} MHz) is still slow with respect to the interaction frequency.[33] This is consistent with MHz-scale coupling between the components of **3** and **4** (see DEER section).

Note that low-frequency ESEEM effects (<10 MHz) are observed in the primary echo decay experiments of **3** and **4** when monitoring the $\{CrNi_2\}$ components (20 and 40 ns ${}^{\pi}/_2$ and π pulses, respectively), but not on the $\{Cr_7Ni\}$ components. The fact that they are only observed on the $\{CrNi_2\}$ resonances implies that they are due to the ^{14}N of the $\{CrNi_2\}$-bound pyridyl groups (Larmor frequency 3.03 MHz at B_0 = 983 mT).

Structures in Three Phases and at Three Temperatures. DEER spectroscopy gives us spin···spin distances at 3 K in a dilute frozen solution. Triangular, organic three-spin systems have been studied previously by DEER (with one arm missing in the biradical system), and the effect of three-spin correlations on the distance distribution data examined by comparison to equivalent two-spin molecules, where one arm of the triangle is missing.[31,34] In **3** and **4**, we have analogues of such systems but based on delocalized multicenter spin systems. Here, we are measuring $\{Cr_7Ni\}$ ring···ring contacts. From the AMDS calculations we also have a structure in a mobile solution at 300 K (confirmed by the SAXS measurement, Figure 2). From single-crystal diffraction we have a structure at 200 K in a crystalline material. It is interesting to compare these three structures of **3** and **4** (Figure 6, Table 3).

We make the assumption that the electron spin on the $\{Cr_7Ni\}$ rings in **3** and **4** sits on the metal sites. The DEER analysis is therefore giving us the distribution of inter-ring M··· M distances in frozen solution at 3 K. We are not seeing any metal···metal contacts involving the central $\{CrNi_2\}$ triangle (see above). We first used DeerAnalysis software[27] using

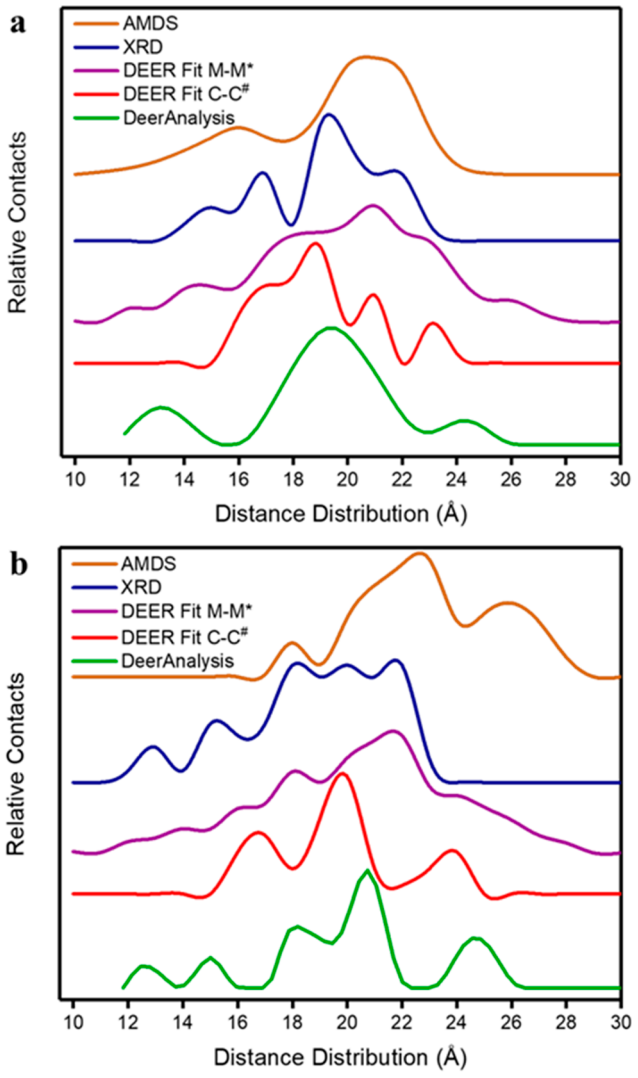

Figure 6. Distribution of inter-$\{Cr_7Ni\}$ metal···metal contacts by three methods, in (a) **3** and (b) **4**. AMDS calculation (brown); XRD (dark blue); metal-to-metal (purple) and centroid-to-centroid (red) distances found by iterative fit of DEER data; fit from DeerAnalysis (Tikhonov regularizations; green). The AMDS distances were calculated using the center of mass of the atoms involved and calculated for every time step over 10 ns; the average was then taken throughout the simulation to determine the distances. The XRD distances between metal ions for each $\{Cr_7Ni\}$···$\{Cr_7Ni\}$ are plotted in 0.5 Å increments using a spline function. The DEER data are taken directly from the distance distributions in Figures 4 and 5

Table 3. Maxima (Å) in Distribution of Intra-ring M···M Distances

3	AMDS	16.0	20.7					
	XRD	15.0	16.9	19.3	21.1			
	DEER[a]	12.1	14.5	17.9	20.9	22.9	26.0	
	DEER[b]	13.1	19.4	24.4				
4	AMDS	18.0	22.7	26.9				
	XRD	12.9	15.2	18.2	20.0	21.8		
	DEER[a]	12.0	13.9	16.0	18.0	21.7	24.2	25.8
	DEER[b]	12.7	15.0	18.1	20.7	24.7		

[a]M···M DEER fit. [b]DeerAnalysis.

https://dx.doi.org/10.1021/jacs.0c06547
J. Am. Chem. Soc. 2020, 142, 15941−15949

Tikhonov regularizations[26] to calculate a distance distribution based on dipolar coupling. DeerAnalysis assumes an average nitroxide g value, and a correction factor is required based on the g values of the experimental pump and observation pulses (1.76 and 1.77, respectively): this results in shifts to slightly shorter distances. The more significant difference here is that the spin on each {Cr_7Ni} ring is distributed across eight sites.[35] Therefore, in **3** we have contacts between three sets of eight sites and in **4** we have contacts between two sets of eight sites. Such effects can lead to deviations in distance distributions based on point-dipole models and the cluster centroids, as has been shown with biological FeS clusters.[36]

Hence, we also fit the DEER data with a structural model, allowing for distribution of the spin over the eight sites of the {Cr_7Ni} rings and accounting for orientation selection due to the g anisotropy. In Figures 4c and 5c, we compare the distance distributions extracted from the conformer library, presented both as M···M distances and as ring centroid··· centroid distances, with those obtained from model-free DeerAnalysis. It is striking that, for both **3** and **4**, the DEER fit centroid···centroid distribution strongly resembles the DeerAnalysis results in terms of the dominant distances, with the exception that the DeerAnalysis distributions (a) are shifted to longer distances by 1−2 Å and (b) pick up short distances (<15 Å) that are not found in the centroid···centroid distribution.

The agreement, despite the neglect of DEER orientation selectivity in {Cr_7Ni} due to g aniostropy,[25] is because the rings are essentially axially symmetric and we are pumping at $g_{x,y}$. In this case we will always detect the perpendicular component of the dipolar coupling pattern, such that a single DEER measurement can yield reasonable distance distributions obtained from Tikhonov regularizations.[28,37] We have tested and validated this assumption by simulation (see Supporting Information).

For both **3** and **4**, the DEER fit M···M distance distributions are broader than either the centroid···centroid or DeerAnalysis results, notably picking up the shorter distances (<15 Å) and extending to longer distances (>25 Å). The closer agreement between the DeerAnalysis and DEER fit centroid···centroid distributions is likely a result of the fact that DeerAnalysis uses the point dipole approach, and given that the spin is evenly distributed around the {Cr_7Ni} ring (once positional disorder of the Ni(II) ion is considered), this seems to average out to give distances similar to a spin localized at the center of the ring.

For **3** the distance distribution from DeerAnalysis has three maxima (Figure 6a), at 13.1 Å (toward the lower end of distances that can be measured by DEER),[38,39] a dominant peak at 19.4 Å, and a smaller peak at around 24.4 Å. The DEER fit M···M distribution gives peaks between 12 and 26 Å, with the bulk of contacts between 18 and 24 Å (Figure 6a).

To compare this with the inter-ring M···M distances in **3** as observed by single crystal X-ray diffraction, we have arranged the M···M distances from diffraction in distributions of 0.5 Å and then broadened the distribution (dark blue line in Figure 6a). There are two maxima at 15.0 and 16.9 Å, reflecting the rings being arranged in an isosceles triangle in the crystal. There is then a gap in the distribution before we reach a maximum at 19.3 Å, consistent with the broad maximum in the DEER fit M···M data and the maximum in the DeerAnalysis distribution. There is then a small fall before a peak at 21.1 Å.

If we then compare with the AMDS structure (brown line in Figure 6a), we see a very similar shape to the DeerAnalysis distribution, but shifted to longer distances with two maxima at 16.0 and 20.7 Å. The simpler distribution from AMDS cf. XRD suggests that the structure in fluid solution is relaxing to an equilateral triangle of rings compared to the crystal structure. The DEER fit M···M distribution is more complex, with shorter and longer distances, reflecting the fact that a number of conformations are trapped on freezing the solution, and there are also possible differences in librational effects due to the extreme difference in temperatures of measurement (3 and 300 K). Some of this detail is lost in the simpler DeerAnalysis treatment. However, the dominant DEER fit M···M distances around 21 Å agree with that from AMDS.

The conclusion is that in fluid solution at room temperature **3** has a structure where the rings in the three [2]-rotaxanes form an equilateral triangle. Additional structure is seen in the XRD as packing leads to a change in the overall structure toward an isosceles triangle, but with similar size. While a range of conformations are found in the frozen solution at 3 K, the dominant distances are similar to the fluid solution.

For compound **4** the result is very different (Figure 6b). The XRD distance distribution has a similar longest distance at 22 Å, cf. 21 Å for **3**. However, there are significantly shorter contacts at 13 Å, cf. 15 Å in **3**. In **4** the AMDS and XRD structures are radically different from one another. In AMDS the shortest contact has a maximum at 18.0 Å, with the shortest contacts found in XRD and DEER (see below) entirely missing. The majority of M···M contacts by AMDS are around 22.7 Å, around the longest contact from XRD and the dominant contact by DEER fit. Finally, the AMDS has a much longer and significant contact at above 26 Å, which is absent in the XRD. Hence, the AMDS structure is much more extended than the structure as observed by crystallography.

The DeerAnalysis distance distribution for **4** gives short distances at 12.7 and 15.0 Å, the majority of contacts from 17.5 to 21.9 Å, and a long-distance peak at 24.7 Å. The DEER fit M···M distribution gives peaks between the shortest and longest distances of 12 and 28 Å, with the dominant peak at around 22 Å. Comparing these to equivalent data for **3**, both analyses show that in **4** there is a broader distance distribution, extending to longer distances, in the frozen solution. The DEER fit M···M distribution for **4** appears to combine features of those from the XRD and AMDS, with the short distances from the former and the long distances from the latter. However, although the M···M DEER fit result contains distances that extend beyond those found in the AMDS distributions, the dominant distance is significantly shorter.

All these results say that the [3]-rotaxane (**4**) relaxes much more in solution than the [4]-rotaxane (**3**). The presence of only two large [2]-rotaxanes attached to the central triangle in **4** leads to steric repulsion between these groups. The result is a bigger structure in mobile solution (also shown by the radius of gyration data, see Supporting Information) and also a broader range of conformations on freezing the solutions as shown by DEER. Hence, the fluid and frozen solution structures differ more significantly from each other for **4** than for **3**.

CONCLUSION

We have prepared two large supramolecular assemblies **3** and **4**, containing 27 and 19 paramagnetic centers, respectively. Single-crystal diffraction studies allow us to show these are [4]-

https://dx.doi.org/10.1021/jacs.0c06547
J. Am. Chem. Soc. 2020, 142, 15941−15949

and [3]-rotaxanes with three or two $\{Cr_7Ni\}$ rings attached to a central $\{CrNi_2\}$ triangle.

Such huge molecules have many degrees of freedom, and by analyzing AMDS structures calculated in solution, confirmed by SAXS data, we can see that the symmetric [4]-rotaxane behaves very differently from the asymmetric [3]-rotaxane. The packing of the [4]-rotaxane in the crystal leads to an isosceles triangle of $\{Cr_7Ni\}$ rings that is not seen in solution by SAXS/AMDS. Here, the crystallography establishes connectivity but not the conformation in solution, while DEER shows a relatively narrow range of conformations in the frozen solution. For the asymmetric [3]-rotaxane we find that the structural differences in solution, fluid and frozen, are much greater in terms of both the extension of the molecule and the range of conformations observed.

Determining such details of the structure of very large paramagnetic assemblies is very difficult as the line broadening due to paramagnetism vitiates the use of NMR spectroscopy. Here, the combination of AMDS and DEER allows us to characterize the materials and their conformers from 3 to 300 K.

■ ASSOCIATED CONTENT

Supporting Information

The Supporting Information is available free of charge at https://pubs.acs.org/doi/10.1021/jacs.0c06547.

Experimental section; crystallography; c.w. EPR data; EDFS data; relaxation data; M···M distance distribution from XRD; SAXS data; DEER modeling including orientation selection effects and structural model fitting; multispin analysis (PDF)

X-ray crystallographic data for **4** (CIF)

X-ray crystallographic data for **3** (CIF)

■ AUTHOR INFORMATION

Corresponding Authors

Eric J. L. McInnes − *Department of Chemistry and Photon Science Institute, The University of Manchester, Manchester M13 9PL, U.K.*; orcid.org/0000-0002-4090-7040; Email: eric.mcinnes@manchester.ac.uk

Richard E. P. Winpenny − *Department of Chemistry and Photon Science Institute, The University of Manchester, Manchester M13 9PL, U.K.*; orcid.org/0000-0002-7101-3963; Email: richard.winpenny@manchester.ac.uk

Authors

Selena J. Lockyer − *Department of Chemistry and Photon Science Institute, The University of Manchester, Manchester M13 9PL, U.K.*

Selina Nawaz − *Department of Chemistry and Photon Science Institute, The University of Manchester, Manchester M13 9PL, U.K.*

Adam Brookfield − *Department of Chemistry and Photon Science Institute, The University of Manchester, Manchester M13 9PL, U.K.*

Alistair J. Fielding − *School of Pharmacy and Biomolecular Sciences, Liverpool John Moores University, Liverpool L3 3AF, U.K.*; orcid.org/0000-0002-4437-9791

Inigo J. Vitorica-Yrezabal − *Department of Chemistry and Photon Science Institute, The University of Manchester, Manchester M13 9PL, U.K.*

Grigore A. Timco − *Department of Chemistry and Photon Science Institute, The University of Manchester, Manchester M13 9PL, U.K.*

Neil A. Burton − *Department of Chemistry and Photon Science Institute, The University of Manchester, Manchester M13 9PL, U.K.*

Alice M. Bowen − *Department of Chemistry and Photon Science Institute, The University of Manchester, Manchester M13 9PL, U.K.*; orcid.org/0000-0002-6413-2841

Complete contact information is available at: https://pubs.acs.org/10.1021/jacs.0c06547

Author Contributions

The manuscript was written through contributions of all authors. All authors have given approval to the final version of the manuscript.

Funding

This work was supported by the EPSRC through the award of a doctoral training grant to S.J.L. and funding of the EPSRC National EPR Facility at Manchester (NS/A000055/1). This work was supported by the EPSRC(UK) (Grant No. EP/L018470/1) and a Established Career Fellowship (EP/R011079/1) to R.E.P.W. We also thank EPSRC (UK) for funding an X-ray diffractometer (EP/K039547/1). We also thank the European Research Council for an Advanced Grant (ERC-2017-ADG-786734). We thank Diamond Light Source for access to synchrotron X-ray facilities. A.M.B. thanks the Royal Society and EPSRC for a Dorothy Hodgkin Fellowship (DH160004).

Notes

The authors declare no competing financial interest.

■ DEDICATION

We dedicate this paper to Professor Alan J. Welch on the occasion of his retirement.

■ REFERENCES

(1) Ueda, Y.; Ito, H.; Fujita, D.; Fujita, M. Permeable Self-Assembled Molecular Contains for Catalysis Isolation Enabling Two-Step Cascade Reactions. *J. Am. Chem. Soc.* **2017**, *139* (17), 6090−6093.

(2) Saha, R.; Devaraj, A.; Bhattacharyya, S.; Das, S.; Zangrando, E.; Mukherjee, P. S. Unusual Behaviour of Donor-Acceptor Stenhouse Adducts (DASA) in Confined Space of a Water Soluble $Pd^{II}8$ Molecular Vessel. *J. Am. Chem. Soc.* **2019**, *141*, 8638−8645.

(3) Mal, P.; Breiner, B.; Rissanen, K.; Nitschke, J. R. White Phosphorus Is Air-Stable Within a Self-Assembled Tetrahedral Capsule. *Science* **2009**, *324*, 1697−1699.

(4) Fahrenbach, A. C.; Bruns, C. J.; Li, H.; Trabolsi, A.; Coskun, A.; Stoddart, J. F. Ground-State Kinetics of Bistable Redox-Active Donor−Acceptor Mechanically Interlocked Molecules. *Acc. Chem. Res.* **2014**, *47*, 482−493.

(5) Zhang, L.; Stephens, A. J.; Lemonnier, J.-F.; Pirvu, L.; Vitorica-Yrezabal, I. J.; Robinson, C. J.; Leigh, D. A. Coordination Chemistry of a Molecular Pentafoil Knot. *J. Am. Chem. Soc.* **2019**, *141*, 3952−3958.

(6) Zhang, L.; Stephens, A. J.; Nussbaumer, A. L.; Lemonnier, J.-F.; Jurček, P.; Vitorica-Yrezabal, I. J.; Leigh, D. A. Stereoselective synthesis of a composite knot with nine crossings. *Nat. Chem.* **2018**, *10*, 1083−1088.

(7) Zhang, L.; Lemonnier, J.-F.; Acocella, A.; Calvaresi, M.; Zerbetto, F.; Leigh, D. A. Effects of knot tightness at the molecular level. *Proc. Natl. Acad. Sci. U. S. A.* **2019**, *116*, 2452−2457.

(8) Sprafke, J. K.; Kondratuk, D. V.; Wykes, M.; Thompson, A. L.; Hoffmann, M.; Drevinskas, R.; Chen, W.; Yong, C. K.; Kärnbratt, J.; Bullock, J. E.; Malfois, M.; Wasielewski, M. R.; Albinsson, B.; Herz, L. M.; Zigmantas, D.; Beljonne, D.; Anderson, H. L. Belt-Shaped π-Systems: Relating Geometry to Electronic Structure in a Six-Porphyrin Nanoring. *J. Am. Chem. Soc.* **2011**, *133*, 17262−17273.
(9) Tiede, D. M.; Zhang, R.; Chen, L. X.; Yu, L.; Lindsey, J. S. Structural characterization of modular supramolecular architectures in solution. *J. Am. Chem. Soc.* **2004**, *126* (43), 14054−14062.
(10) Ferrando-Soria, J.; Fernandez, A.; Asthana, D.; Nawaz, S.; Vitorica-Yrezabal, I. J.; Whitehead, G. F. S.; Muryn, C. A.; Tuna, F.; Timco, G. A.; Burton, N. D.; Winpenny, R. E. P. A [13]rotaxane assembled via a palladium molecular capsule. *Nat. Commun.* **2019**, *10*, 3720.
(11) Fernandez, A.; Ferrando-Soria, J.; Pineda, E. M.; Tuna, F.; Vitorica-Yrezabal, I. J.; Knappke, C.; Ujma, J.; Muryn, C.; Timco, G. A.; Barran, P. E.; Ardavan, A.; Winpenny, R. E. P. Making hybrid [n]-rotaxanes as supramolecular arrays of molecular electron spin qubits. *Nat. Commun.* **2016**, *7*, 10240.
(12) Ferrando-Soria, J.; Moreno Pineda, E.; Chiesa, A.; Fernandez, A.; Magee, S. A.; Carretta, S.; Santini, P.; Vitorica-Yrezabal, I. J.; Tuna, F.; Timco, G. A.; McInnes, E. J.L.; Winpenny, R. E.P. A modular design of molecular qubits to implement universal quantum gates. *Nat. Commun.* **2016**, *7*, 11377.
(13) Fernandez, A.; Moreno Pineda, E.; Muryn, C. A.; Sproules, S.; Moro, F.; Timco, G. A.; McInnes, E. J. L.; Winpenny, R. E. P. g-Engineering in Hybrid Rotaxanes To Create AB and AB_2 Electron Spin Systems: EPR Spectroscopic Studies of Weak Interactions between Dissimilar Electron Spin Qubits. *Angew. Chem., Int. Ed.* **2015**, *54*, 10858−10861.
(14) Lockyer, S. J.; Fielding, A. J.; Whitehead, G. F. S.; Timco, G. A.; Winpenny, R. E. P.; McInnes, E. J. L. Close encounters of the weak kind: investigations of electron-electron interactions between dissimilar spins in hybrid rotaxanes. *J. Am. Chem. Soc.* **2019**, *141*, 14633−14642.
(15) Walsh, J. P. S.; Meadows, S. B.; Ghirri, A.; Moro, F.; Jennings, M.; Smith, W. F.; Graham, D. M.; Kihara, T.; Nojiri, H.; Vitorica-Yrezabal, I. J.; Timco, G. A.; Collison, D.; McInnes, E. J. L.; Winpenny, R. E. P. Electronic Structure of a Mixed-Metal Fluoride-Centered Triangle Complex: A Potential Qubit Component. *Inorg. Chem.* **2015**, *54*, 12019−12026.
(16) Whitehead, G. F. S.; Cross, B.; Carthy, L.; Milway, V. A.; Rath, H.; Fernandez, A.; Heath, S. L.; Muryn, C. A.; Pritchard, R. G.; Teat, S. J.; Timco, G. A.; Winpenny, R. E. P. Rings and threads as linkers in metal−organic frameworks and poly-rotaxanes. *Chem. Commun.* **2013**, *49*, 7195−7197.
(17) Berendsen, H. J. C.; van der Spoel, D.; van Drunen, R. GROMACS: A message-passing parallel molecular dynamics implementation. *Comput. Phys. Commun.* **1995**, *91*, 43−56.
(18) Lindahl, E.; Hess, B.; van der Spoel, D. GROMACS 3.0: A package for molecular simulation and trajectory analysis. *J. Mol. Model.* **2001**, *7*, 306−317.
(19) Cornell, W. D.; Cieplak, P.; Bayly, C. I.; Gould, I. R.; Merz, K. M.; Ferguson, D. M.; Spellmeyer, D. C.; Fox, T.; Caldwell, J. W.; Kollman, P. A. A Second Generation Force Field for the Simulation of Proteins, Nucleic Acids, and Organic Molecules. *J. Am. Chem. Soc.* **1995**, *117*, 5179−5197.
(20) Stoll, S.; Schweiger, A. EasySpin, a comprehensive software package for spectral simulation and analysis in EPR. *J. Magn. Reson.* **2006**, *178*, 42.
(21) Timco, G. A.; Faust, T. B.; Tuna, F.; Winpenny, R. E. P. Linking heterometallic rings for quantum information processing and amusement. *Chem. Soc. Rev.* **2011**, *40*, 3067−3075.
(22) Schiemann, O.; Prisner, T. F. Long-range distance determinations in biomacromolecules by EPR spectroscopy. *Q. Rev. Biophys.* **2007**, *40*, 1−53.
(23) Jeschke, G.; Polyhach, Y. Distance Measurements on Spin-Labelled Biomacromolecules by Pulsed Electron Paramagnetic Resonance. *Phys. Chem. Chem. Phys.* **2007**, *9*, 1895−1910.
(24) Abdullin, D.; Schiemann, O. Pulsed dipolar EPR spectroscopy and metal ions: methodology and biological applications. *ChemPlusChem* **2020**, *85*, 353.
(25) Ardavan, A.; Bowen, A. M.; Fernandez, A.; Fielding, A. J.; Kaminski, D.; Moro, F.; Muryn, C. A.; Wise, M. D.; Ruggi, A.; McInnes, E. J. L.; Severin, K.; Timco, G. A.; Timmel, C. R.; Tuna, F.; Whitehead, G. F. S.; Winpenny, R. E. P. Engineering coherent interactions in molecular nanomagnet dimers. *npj Quantum Information* **2015**, *1*, 15012.
(26) Weese, J. A reliable and fast method for the solution of Fredhol integral equations of the first kind based on Tikhonov regularization. *Comput. Phys. Commun.* **1992**, *69*, 99−111.
(27) Jeschke, G.; Chechik, V.; Ionita, P.; Godt, A.; Zimmermann, H.; Banham, J.; Timmel, C. R.; Hilger, D.; Jung, H. DeerAnalysis2006. *Appl. Magn. Reson.* **2006**, *30*, 473−498.
(28) Lovett, J. E.; Bowen, A. M.; Timmel, C. R.; Jones, M. W.; Dilworth, J. R.; Caprotti, D.; Bell, S. G.; Wong, L. L.; Harmer, J. Structural information from orientationally selective DEER spectroscopy. *Phys. Chem. Chem. Phys.* **2009**, *11*, 6840−6848.
(29) Marko, A.; Prisner, T. F. An algorithm to analyse PELDOR data of rigid spin label pairs. *Phys. Chem. Chem. Phys.* **2013**, *15*, 619−627.
(30) von Hagens, T.; Polyhach, Y.; Sajid, M.; Godt, A.; Jeschke, G. Suppresion of ghost distances in multiple-spin double electron-electron resonance. *Phys. Chem. Chem. Phys.* **2013**, *15*, 5854−5866.
(31) Bode, B.; Margraf, D.; Plackmeyer, J.; Dürner, G.; Prisner, T. F.; Schiemann, O. Counting the monomers in nanometer sized oligomers by pulsed electron-electron double resonance. *J. Am. Chem. Soc.* **2007**, *129*, 6736−6745.
(32) Burchfield, J. M.; Du, J. L.; More, K. M.; Eaton, S. S.; Eaton, G. R. Enhancement of electron spin relaxation rates of metalloporphyrins due to interaction with a faster relaxing metal bound to an appended bipyridyl. *Inorg. Chim. Acta* **1997**, *263*, 23−33.
(33) Rakowsky, M. H.; More, K. M.; Kulikov, A. V.; Eaton, G. R.; Eaton, S. S. Time domain electron paramagnetic resonance as a probe of electron-electron spin-spin interaction in spin-labelled low-spin iron porphyrins. *J. Am. Chem. Soc.* **1995**, *117*, 2049−2057.
(34) Jeschke, G.; Sajid, M.; Schulte, M.; Godt, A. Three-spin correlations in double electron−electron resonance. *Phys. Chem. Chem. Phys.* **2009**, *11*, 6580−6591.
(35) Casadei, C. M.; Bordonali, L.; Furukawa, Y.; Borsa, F.; Garlatti, E.; Lascialfari, A.; Carretta, S.; Sanna, S.; Timco, G. T. A.; Winpenny, R. E. P. Local spin density in the Cr_7Ni antiferromagnetic molecular ring and ^{53}Cr-NMR. *J. Phys.: Condens. Matter* **2012**, *24*, 406002.
(36) Elsasser, C.; Brecht, M.; Bittl, R. Pulsed electron-electron double resonance on multinuclear metal clusters: assignment of spin projection factors based on the dipolar interaction. *J. Am. Chem. Soc.* **2002**, *124*, 12606−12611.
(37) Bowen, A. M.; Tait, C. E.; Timmel, C. R.; Harmer, J. R. Orientation-Selective DEER Using Rigid Spin Labels, Cofactors, Metals, and Clusters. In *Structural Information from Spin-Labels and Intrinsic Paramagnetic Centres in the Biosciences. Structure and Bonding*; Timmel, C., Harmer, J., Eds.; Springer: 2013; Vol. *152*, pp 283−327.
(38) Jeschke, G. Determination of the Nanostructure of Polymer Materials by Electron Paramagnetic Resonance Spectroscopy. *Macromol. Rapid Commun.* **2002**, *23*, 227−246.
(39) Bowen, A. M.; Jones, M. W.; Lovett, J. E.; Gaule, T. G.; McPherson, M. J.; Dilworth, J. R.; Timmel, C. R.; Harmer, J. R. Exploiting orientation-selective DEER: determining molecular structure in systems containing Cu(II) centres. *Phys. Chem. Chem. Phys.* **2016**, *18*, 5981−5994.

https://dx.doi.org/10.1021/jacs.0c06547
J. Am. Chem. Soc. 2020, 142, 15941−15949